nature physics

SUPPLEMENTARY INFORMATION
https://doi.org/10.1038/s41567-018-0363-x

In the format provided by the authors and unedited.

Strain-tunable magnetism at oxide domain walls

D. V. Christensen[1,7], Y. Frenkel[2,7], Y. Z. Chen[1], Y. W. Xie[3,4,5], Z. Y. Chen[3,4], Y. Hikita[3], A. Smith[1], L. Klein[6], H. Y. Hwang[3,4], N. Pryds[1*] and B. Kalisky[2*]

[1]Department of Energy Conversion and Storage, Technical University of Denmark, Roskilde, Denmark. [2]Department of Physics and Institute of Nanotechnology and Advanced Materials, Bar-Ilan University, Ramat-Gan, Israel. [3]Stanford Institute for Materials and Energy Sciences, SLAC National Accelerator Laboratory, Menlo Park, CA, USA. [4]Department of Applied Physics, Geballe Laboratory for Advanced Materials, Stanford University, Stanford, CA, USA. [5]Department of Physics, Zhejiang University, Hangzhou, China. [6]Department of Physics, Nano-magnetism Research Center, Institute of Nanotechnology and Advanced Materials, Bar-Ilan University, Ramat-Gan, Israel. [7]These authors contributed equally: D. V. Christensen, Y. Frenkel.
*e-mail: nipr@dtu.dk; beena@biu.ac.il

Supplementary material for

Strain tunable magnetism at oxide domain walls

D. V. Christensen[1†], Y. Frenkel[2†], Y. Z. Chen[1], Y. Xie[3,4,5], Z. Chen[4], Y. Hikita[3], A. Smith[1], L. Klein[6], H. Y. Hwang[3], N. Pryds[1], and B. Kalisky[2*]*

[1] *Department of Energy Conversion and Storage, Technical University of Denmark, Risø Campus, DK-4000 Roskilde, Denmark.*
[2] *Department of Physics and Institute of Nanotechnology and Advanced Materials, Bar-Ilan University, Ramat-Gan 5290002, Israel.*
[3] *Stanford Institute for Materials and Energy Sciences, SLAC National Accelerator Laboratory, Menlo Park, California 94025, USA*
[4] *Department of Applied Physics, Geballe Laboratory for Advanced Materials, Stanford University*
[5] *Department of Physics, Zhejiang University, Hangzhou, 310027, China*
[6] *Department of Physics, Nano-magnetism Research Center, Institute of Nanotechnology and Advanced Materials, Bar-Ilan University, Ramat-Gan, 5290002 Israel.*

† These authors contributed equally to this work

* Email: nipr@dtu.dk and beena@biu.ac.il.

Table of contents

The PDF file contains:

Section 1:
Materials, methods and magnetic impurities

Sample preparation:
The LAO/STO and GAO/STO heterostructures were prepared from TiO_2-terminated STO using standard protocols for the two heterostructures with details found in Ref. (*1*) and (*2*). Importantly, 5 unit cells of LAO were deposited on STO at 800 °C in an oxygen pressure of 10^{-5} mbar and cooled down to 600 °C, where the sample was annealed in an atmosphere of 0.4 bar oxygen for one hour. The GAO film was deposited on STO at 650 °C in an oxygen pressure of 10^{-5} mbar and cooled down to room temperature in the deposition pressure in absence of an annealing step. The STO substrates were exposed to the same conditions as the GAO/STO heterostructure, except for the deposition.

Transport measurements:
The buried interfaces were contacted by wedge-bonding with aluminum wires in the van der Pauw geometry to avoid influence of patterning the interface into Hall-bars. The magnetoresistance and Hall resistance were symmetrized and antisymmetrized, respectively, prior to the analysis to minimize spurious intermixing. The main features remained unchanged by symmetrization. The transport measurements were conducted from room temperature to 2 K in magnetic fields up to 15 T with standard DC measurements with a typical probing current of 10 μA. No hysteresis was detected in the magnetoresistance or the Hall resistance.

Scanning-SQUID measurements:
The scanning SQUID system is a custom-built piezoelectric-based scanning SQUID microscope with a 1.8 μm diameter pick-up loop (*3*, *4*). We used the scanning SQUID to image magnetic flux from the sample as a function of position. The measured magnetic flux is given by $\phi_s = \int g(x,y)\vec{B} \cdot d\vec{a}$ where the integral is taken over the plane of the SQUID, $g(x,y)$ is the point spread function of the pick-up loop, $\vec{B}$ is the background-corrected magnetic field produced by the sample and $d\vec{a}$ is the infinitesimal area vector element pointing normal to the plane of the SQUID. The SQUID was used in three modes: Magnetometry, susceptometry and current detection mode (see Figure S1).
The magnetometry measurements are simply the z component of the magnetic flux, picked up by the SQUID's pick up loop in absence of an applied magnetic field. For the susceptometry measurements we applied a local magnetic field of up to 0.3 mT to the sample using a field coil with a diameter of 8 μm that surrounds the pick-up loop of the SQUID. If the sample magnetization changes upon applying the local magnetic field, the sample itself produces a magnetic field in the pick-up loop that was measured by a standard lock-in technique. An identical field coil surrounds a second pick-up loop used to correct for background magnetic fields in the magnetometry mode (gradiometric design). In current detection mode, an alternating current is applied to the sample and the pickup loop is used to detect the magnetic flux generated by these currents using a lock-in technique. A single current-carrying wire will

appear in our images as a stripe with a negative magnetic signal next to a stripe of a positive signal.

In all measuring modes, the magnetic landscape was imaged by the SQUID loop rastering parallel to the surface at a height down to a micrometer. The contact with the surface was probed capacitively using a cantilever and a fixed electrode. Using the tip of the SQUID probe, we applied forces up to $F = 106$ μN, which corresponds to a pressure of the order of 10^7 Pa, taking into account the estimated contact radius. Following Ref. (*5*), the contact radius (a) was estimated using the Hertzian contact formula:

$$a^3 = \frac{3F}{8} \frac{\frac{(1-\nu_1)}{E_1} + \frac{(1-\nu_2)}{E_2}}{1/d_1}$$

where ν, E, and d are the Poisson ratio, Young's modulus and radius of curvature, respectively. Subscript 1 refers to the silicon tip and subscript 2 is used for the STO substrate.
The imaging is not affected by thin layers of non-conducting materials located between the SQUID and the source of the magnetic field, and the scanning SQUID is therefore an ideal, non-invasive tool to probe magnetism and current paths in buried interfaces.

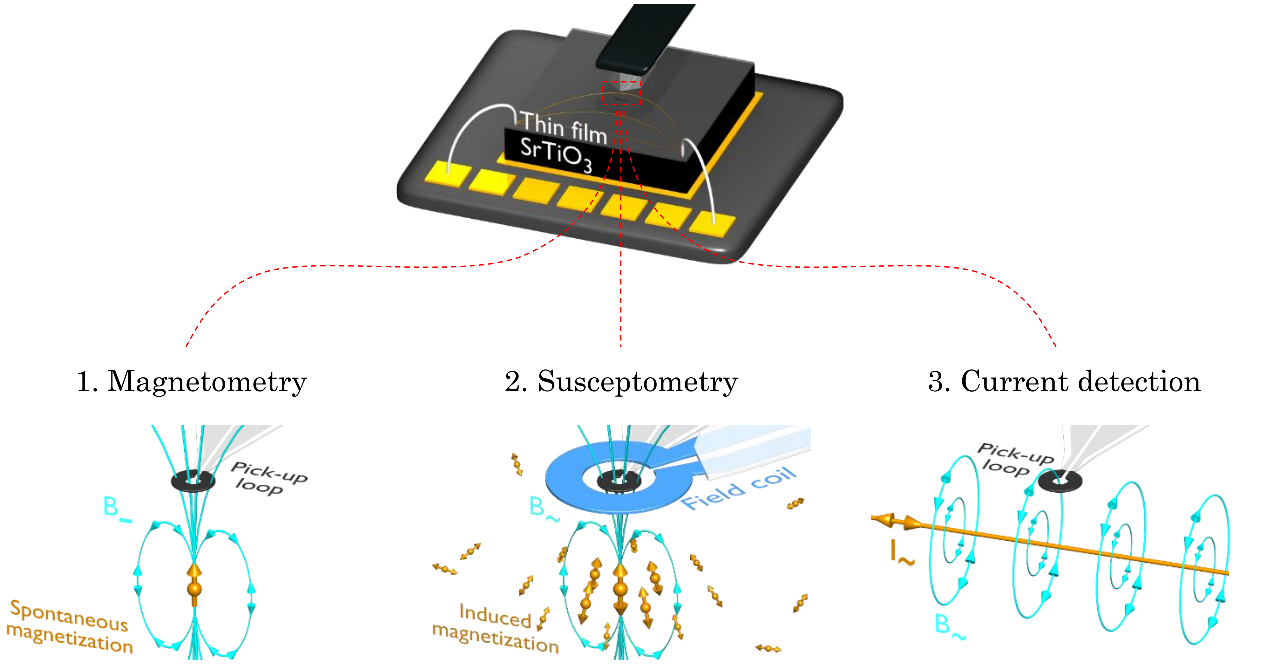

Figure S1: Top: Schematics of the SQUID scanning on the surface of a STO-based material platform. The measurements with the scanning SQUID were performed in three different modes: 1: Magnetometry mode, 2: susceptometry mode and 3: current detection mode.

Magnetic contamination:

Special care was taken to avoid introducing magnetic impurities to the samples throughout the sample preparation, handling and measurements. The samples were handled with non-magnetic plastic tweezers, and the STO was TiO_2-terminated using a tube furnace, glassware and chemicals dedicated to STO treatment. The GAO deposition was done in a pulsed laser deposition chamber dedicated to growing STO-based heterostructures with non-magnetic top layers. The transport and scanning SQUID measurements were conducted using new, thoroughly cleaned chip carriers.

Occasionally, we observe magnetic signals with a similar shape as the resolution limited dipoles observed by Bert et al. (1), but with the ability to be moved on the sample surface using the scanning probe. We attribute these signals to magnetic surface contaminants. In addition, we also sporadically observe signals with the shape of a magnetic dipole buried deep below the sample surface, which we interpret as magnetic impurities or a defect cluster in STO. Lastly, it is well-established that magnetic elements such as Fe, Co and Ni exist in STO (6). We note that special care should be taken to discriminate whether magnetic dipole signals are intrinsic to the sample or stem from magnetic impurities. This is in sharp contrast to the present study where we report 100 μm long magnetic stripes, which are sensitive to applied pressure and change orientation and magnitude upon thermal cycling.

Section 2:
Estimating the magnitude of the magnetization

The magnetization ($\vec{M} = M_x\hat{x} + M_y\hat{y} + M_z\hat{z}$) cannot be calculated uniquely from the measured magnetic flux. The number of Bohr magneton pr. surface unit cell (μ_B/a^2) that create the field can, however, be estimated by assuming that the magnetization is oriented in-plane or out-of-plane. Our estimation uses a simple model where the magnetization is uniform in a sheet with width 2 μm, and zero otherwise. We calculate the field (B_z) at a height of $z = 1$ μm above the sample surface (see Figure S2) using the equation:

$$\vec{B}(\vec{r}) = \frac{\mu_0}{4\pi}\int d\vec{r}'\left(\frac{3\vec{r}(\vec{M}(\vec{r}')\cdot\vec{r})}{|\vec{r}-\vec{r}'|^5} - \frac{\vec{M}(\vec{r}')}{|\vec{r}-\vec{r}'|^3}\right)$$

With this model, we estimate that for the strongest signal we measure (15 mΦ_0 ~ 12μT for GAO/STO as presented in Figure 3 in the main text), a change on the order of 0.7 μ_B/a^2 is needed to create such a field if the magnetization is out-of-plane (see Figure S2c). A similar value is obtained if the magnetization is in-plane (Figure S2b & d). The typical modulation amplitude for GAO/STO (1 mΦ_0, Figure 1 in the main text) corresponds to roughly 0.05 μ_B/a^2.

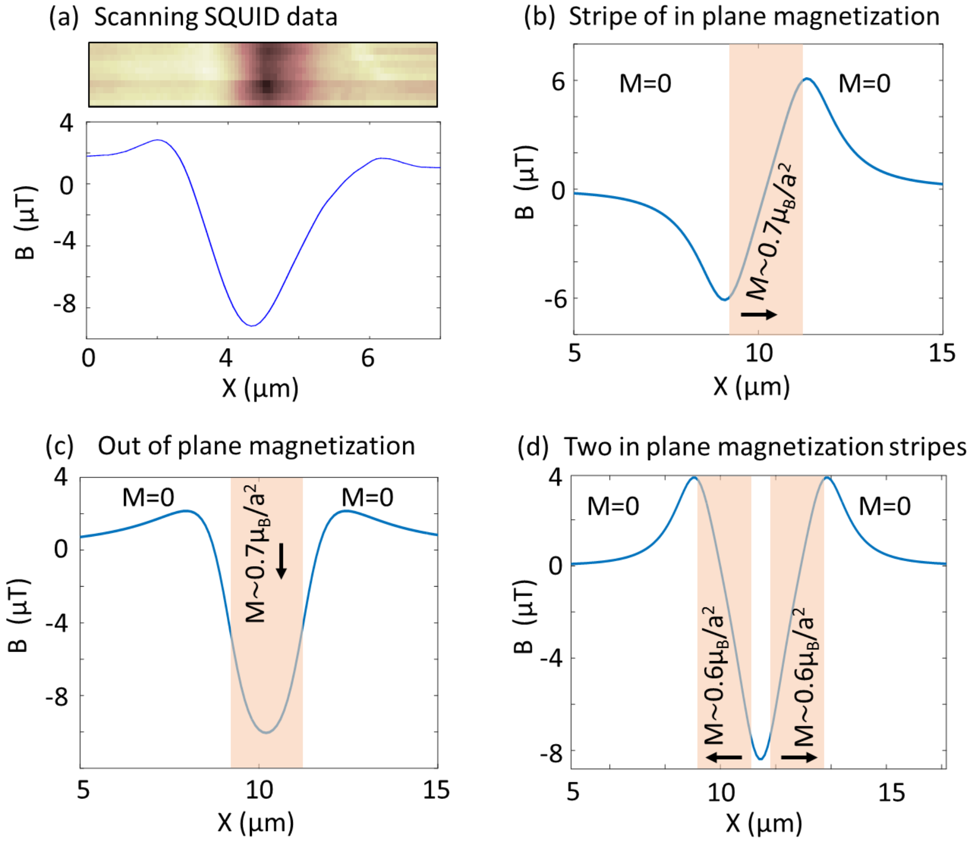

Figure S2: (a) top: SQUID image of the z-component of the magnetic field (B_z) above a magnetic stripe on GAO/STO. Bottom: a line cut along the data. (b), (c) and (d): calculated magnetic field (B_z) over a stripe of in plane (b) and out of plane (c) magnetization. (d): Two in plane magnetic stripes pointing in opposite direction giving rise to a similar B_z. Shaded area in (b), (c) and (d) indicate the location of the $|\vec{M}| \neq 0$ stripes. The magnitude of M in (d) is ~0.6μ_B/a^2 for each stripe.

Section 3:
Magnetic landscape of STO before and after thermal cycling

STO undergoes a structural phase transition at 105K. As the material is cooled through the transition the room temperature cubic unit cell becomes tetragonal. Each unit cell has its long axis along one of the crystallographic directions [001] (*x*), [010] (y) and [100] (*z*), which creates structural domains in STO. At the (001) surface of STO, the domain walls form straight lines along the [100], [010], [110] and [1$\bar{1}$0] directions. The striped magnetic modulations observed in vacuum annealed STO (see Methods) are parallel to these directions (see Figure S3). Heating the material to room temperature and cooling back down to 2 K creates a different magnetic landscape as a different domain structure is formed. Note that the change in the magnetic landscape when performing a temperature cycle helps in ruling out the possibility of the magnetism stemming from contamination.

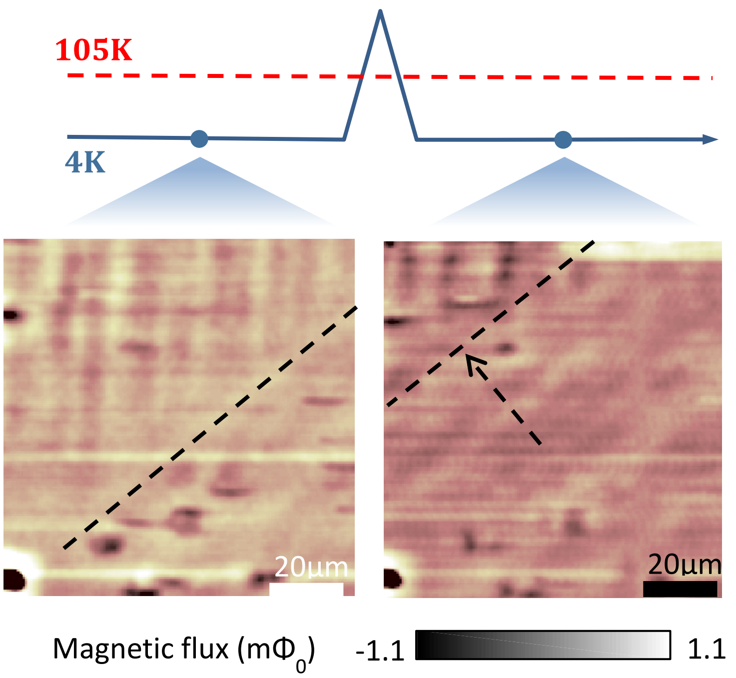

Figure S3: SQUID images of magnetic flux from vacuum-annealed STO before (left) and after (right) a thermal cycling where the sample is warmed up to room temperature. It is notable that the stripy features have changed after the thermal cycle, as indicated by the arrow.

Section 4:
Correlation between stripes in magnetism and current

The structural domain boundaries have been shown to result in a strongly modified current flow in LAO/STO (*7*) and GAO/STO (*8*). Using the current flow and magnetometry modes of the scanning SQUID (see Methods) on the same area of a GAO/STO sample, we observe a clear correlation between the striped current modulations and the magnetic stripes (see Figure S4).

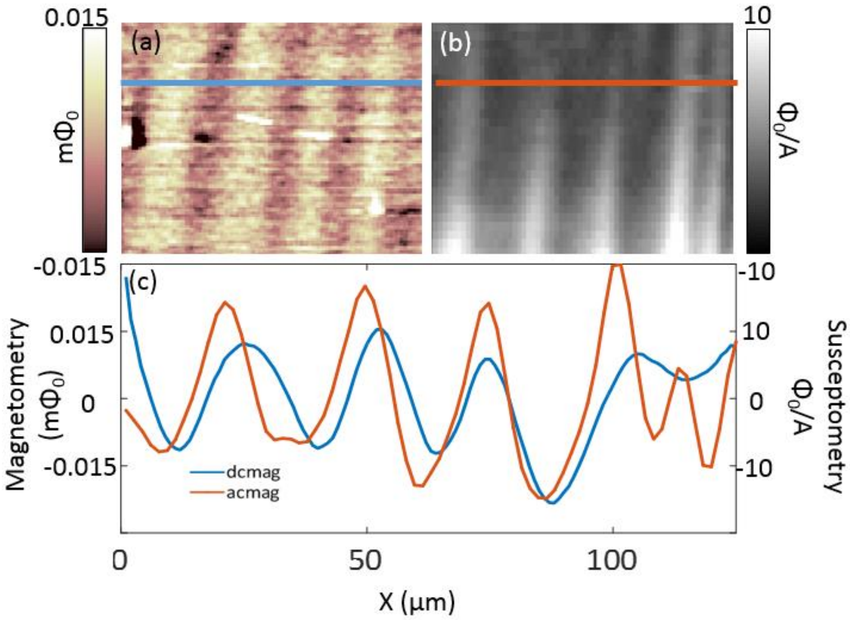

Figure S4: Two consecutive scans of magnetometry (a) and current flow (b) at the same area of GAO/STO showing a similar pattern of stripes. The magnetometry is probed in dc mode with the SQUID by detecting the magnetic field escaping the sample. The current flow is detected in ac mode by applying an alternating current to the GAO/STO sample and measuring the alternating magnetic field produced by the current. (c) Line cuts showing the correlation between the magnetic and current modulations.

Section 5:
Non-linear Hall resistance & 2-band conductivity

If the non-linear Hall resistance (ρ_{xy}) is attributed to conduction through two bands, it can be fitted with the following model (*9*):

$$\rho_{xy} = \frac{\sigma_1^2 R_1 + \sigma_2^2 R_2 + \sigma_1^2 \sigma_2^2 R_1 R_2 (R_1 + R_2) B^2}{(\sigma_1 + \sigma_2)^2 + \sigma_1^2 \sigma_2^2 (R_1 + R_2)^2 B^2} B$$

with the constraint

$$\rho_{xx}(0T) = \frac{1}{\sigma_1 + \sigma_2}$$

and the carrier density ($n_{1,2}$) and carrier mobility ($\mu_{1,2}$) of the two bands defined through

$$\sigma_{1,2} = |n_{1,2} e \mu_{1,2}| \quad \text{and} \quad R_{1,2} = (n_{1,2} e)^{-1}$$

The applicability of a 2-band model to describe the non-linear Hall curves in LAO/STO is discussed extensively in the literature (*10*, *11*). For LAO/STO, the Hall resistance is generally S-shaped, i.e. the Hall resistance curves towards $R_{xy} = 0$, and several reports (*10*, *11*) find that the overall shape of the non-linear Hall resistance is governed by the existence of 2 n-type bands (d_{xy} and d_{xz}/d_{yz}) with different electronic properties. A small non-linear component attributed to the anomalous Hall resistance is, however, present as observed e.g. from the first derivative (dR_{xy}/dB plotted as a function of B) (*11*) or when the external magnetic field is oriented such that only a small field component is normal to the interface (*12*). In the case of GAO/STO, the Hall plots are curve away from $R_{xy} = 0$ (see Figure S5a). Analysis with a 2-band model therefore entails the coexistence of a large density of holes and electrons, as it is also evident from the fitting parameters (see Figure S5b). Such coexistence without a fast recombination is possible if the two types of carriers are separated in real or reciprocal space. However, we reject this scenario on four grounds:

- The GAO/STO has been studied by x-ray absorption spectroscopy (XAS), resonance photoemission spectroscopy (ResPES) and hard x-ray photoemission spectroscopy (HAXPES) without any signature of a band structure that could accommodate holes.
- Large concentrations of co-existing holes and electrons will require a band structure where the Fermi level crosses both an n-type (conduction) and p-type (valence) band, which is challenging to obtain in $SrTiO_3$ owing to its large band gap of approximately 3.2 eV.
- As shown elsewhere (*13*), annealing decreases the Fermi level as a result of lowering the amount of oxygen vacancy donors. An increasing density of holes and decreasing density of electrons are therefore expected from a simple band picture. Experimentally, however, a decrease in both carrier populations is inferred from the 2-band fit as shown in Figure S6.
- Attributing the non-linear Hall effect to the anomalous Hall effect is consistent with scanning SQUID measurements and magnetoresistance measurements as explain in Suppl. Sections 6 and 7.

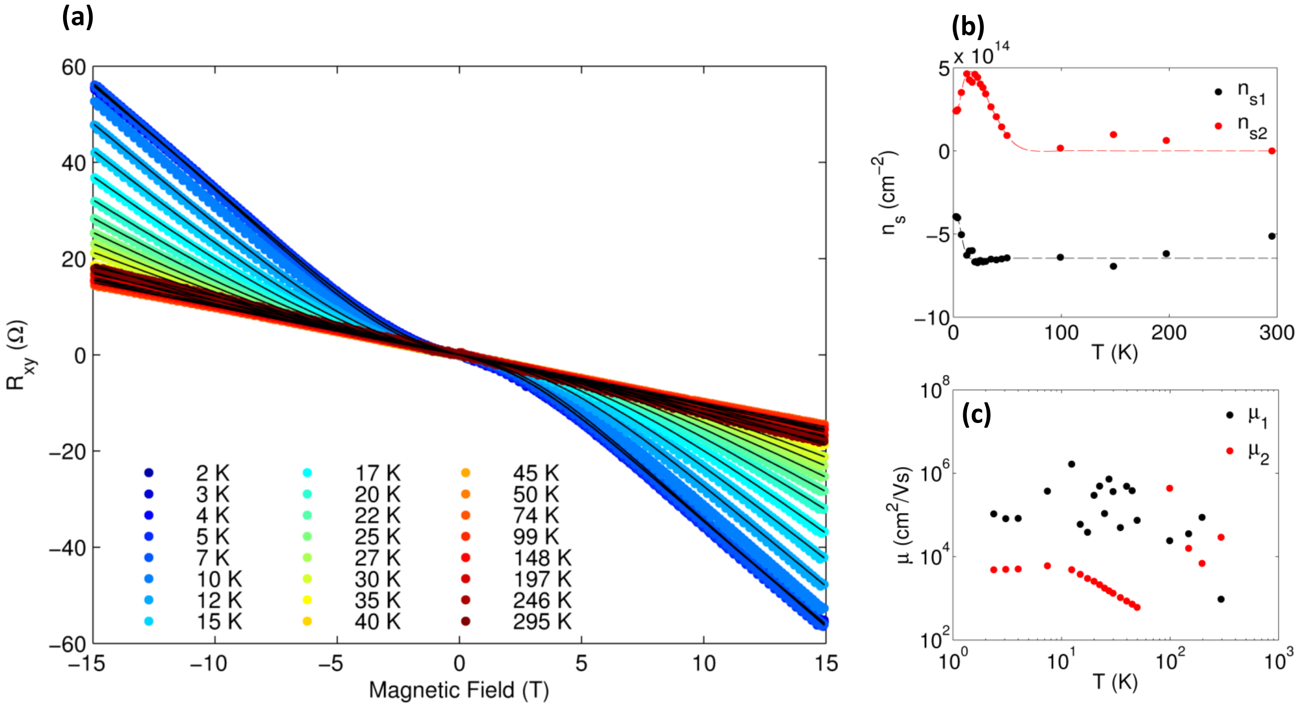

Figure S5: (a) Reasonable fits (black lines) can be obtained by fitting the non-linear Hall resistance R_{xy} of GAO/STO with a 2-band model using (b) the carrier density ($n_{s1,2}$) and (c) mobility ($\mu_{1,2}$) of the two bands as fitting parameters. This require a large number of coexisting electrons ($n_{s1} < 0$) and holes ($n_{s2} > 0$).

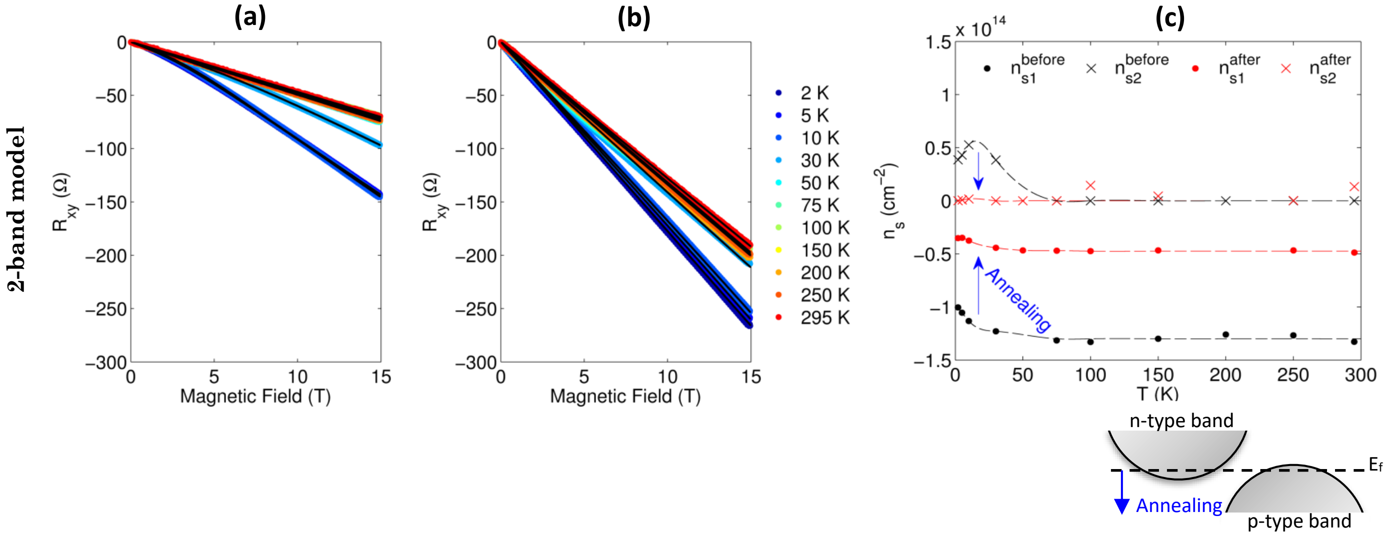

Figure S6: The Hall resistance measured as a function of the external magnetic field (a) before and (b) after annealing GAO/STO in 1 bar oxygen. The Hall resistance is fitted with a 2-band model. (c) The two carrier densities n_{s1} and n_{s2} obtained by the fits are shown as a function of temperature (right pane). The schematic drawing shows the effect of downshifting the Fermi energy level (E_f) by annealing in a bandstructure that can accommodate holes and electrons simulaneously.

Section 6:
Anomalous Hall Effect

As described in the main text, the non-linear Hall resistance of GAO/STO is taken to be a sum of an ordinary Hall effect from a one-band model and the anomalous Hall effect:

$$R_{xy} = R_{xy}^{OHE} + R_{xy}^{AHE} = -\frac{1}{en_s}B + R_s^{AHE}M_z(B,T) \qquad (1)$$

We can now distinguish between two cases according to whether R_s^{AHE} saturates at high magnetic fields or not. For most materials, the anomalous Hall effect saturates at high magnetic fields (*14*). We first argue that whereas this assumption gives reasonable fits, it leads to predictions for the mobility and carrier density that are unlikely. Second, we show that R_s^{AHE} scales with the magnetoresistance, which for GAO/STO does not saturate at high magnetic fields and hence leads to a non-saturating Hall effect.

1: Saturating R_s^{AHE}:

If both R_s^{AHE} and M_z saturate at high magnetic fields of the order of 15 T, the anomalous Hall effect also saturates. In this case, the ordinary Hall contribution and hence the carrier density can be determined from the high-field slope of R_{xy}. Following the treatment by Gunkel et al (*11*), we can describe the magnetization in Eq. (1) with a Langevin-type expression,

$$M_z(B,T) = M_s\tanh(B/B_c')$$

using the saturation magnetization, M_s, and the characteristic magnetic field needed for alignment of magnetic moments, B_c'. Similar fits are obtained if the qualitatively similar Brillouin function is used as appropriate for describing paramagnets with a total angular moment, J, larger than ½:

$$M_z(B,T) = M_s\mathfrak{B}_J(B,T)$$

$$\mathfrak{B}_J(B,T) = \frac{2J+1}{2J}\coth\left(\frac{2J+1}{2J}\frac{g\mu_B JB}{k_B T}\right) - \frac{1}{2J}\coth\left(\frac{1}{2J}\frac{g\mu_B JB}{k_B T}\right)$$

For paramagnets the characteristic magnetic field for aligning the magnetic moments is expected to scale linearly with the temperature. Gunkel et al (*11*), however, found a temperature independent B_c' as expected from an ordered state. As the magnetization curves resembles those derived from the Stoner-Wohlfahrt model, it may be argued that the magnetic equation of states can be used phenomenologically to describe a ferromagnetic state where in-plane magnetic moments are being aligned out-of-plane by the transverse magnetic field (*11*). In the case of GAO/STO, both magnetic equation of states provide good fit. In Figure S7a we present the fits by dotted lines using the Brillouin function ($J > ½$) and a field-independent R_s^{AHE}.

The outcome of describing R_s^{AHE} as field-independent is shown in Figure S7b and c. Note that only J is dependent on the magnetic equation chosen for the fit. B_c is defined as the half maximum at half width (HMHW) of dR_{xy}/dB as in the main text, which gives similar values as the fitting parameter B_c' from the Langevin-type expression. The remaining parameters can be derived from the high-field region where $M_z = M_s$. The temperature dependences of primarily three parameters caution the use of a field-independent R_s^{AHE}:

1. The anomalous Hall saturation ($R_s^{AHE} M_s$) peaks at around 20 K, where for $T < 20$ K a linear correlation with the sheet resistance is observed. This suggests that the skew-scattering underlies anomalous Hall effect (*14*), but in this case R_s^{AHE} is expected to be field-dependent.
2. Extracting the ordinary Hall effect at high magnetic fields implies that the carrier density decreases with a factor of 3-4 when cooling the GAO/STO sample from 100 to 10 K. This is inconsistent with infrared measurements where a temperature-independent carrier density is extracted from the Berreman mode similar to Ref. (*15*).
3. The proposed decrease in the carrier density induces a corresponding increase in the electron mobility, $\mu = 1/eR_s|n_s|$. This would cause the mobility to reach an unprecedented value of ~350,000 cm²/Vs at 2 K. In addition, upon cooling the mobility increases much faster than the $\mu{\sim}T^{-2}$-behavior typically observed in STO and STO-based structures (*11*, *16–18*).

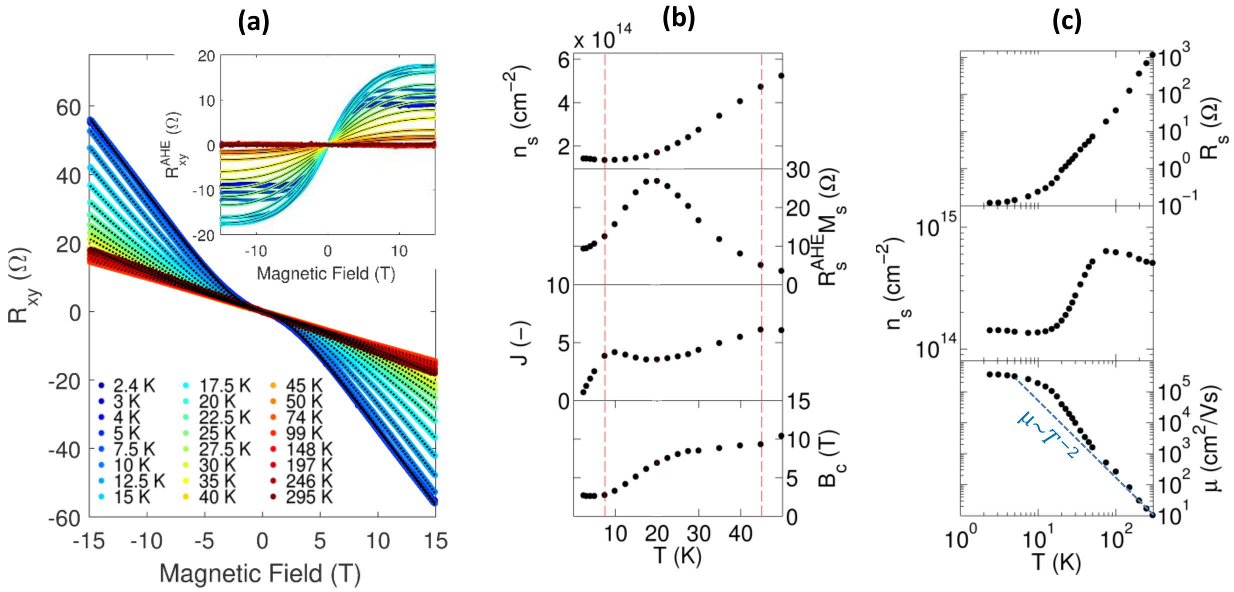

Figure S7: (a) Hall effect (R_{xy}) as a function of the magnetic field including fits (black dots) to Eq. (1) using the Brillouin function and a field-independent R_s^{AHE}. (b+c) Carrier density (n_s), mobility (μ), sheet resistance (R_s), anomalous Hall saturation ($R_s^{AHE} M_s$), total angular momentum (J) and characteristic magnetic field (B_c) as a function of temperature as derived from the description with a field independent R_s^{AHE}.

2: Non-saturating R_s^{AHE}:

We now relax the assumption of a field-independent or saturating R_s^{AHE}. Investigating the case of sample 10a-GAO/STO, we find that the shape of both the Hall resistance and the sheet resistance are very similar with the curvature changing sign at the same magnetic fields (see Figure S8b). This is suggestive of a scenario in which the non-linear Hall resistance arises from the anomalous Hall effect caused by skew scattering where $R_s^{AHE} \propto R_s$, see Ref. (*14*). Here, an asymmetric scattering of electrons occurs in the presence of spin-orbit coupling. According to this hypothesis, we can write:

$$R_{xy} = R_{xy}^{OHE} + R_{xy}^{AHE} = -\frac{1}{en_s}B + kR_s(B,T)M_z(B,T)$$

where k is a field and temperature independent constant and the ordinary Hall effect is described using a one-band model as explained in the main text. At $B \sim 0$ T the sheet resistance is small and scales as B^2, and as a result the anomalous Hall effect becomes small. R_{xy} is therefore dominated by the ordinary Hall effect at low magnetic fields, which offers a natural explanation for the temperature independent Hall slope at low fields, $\left|dR_{xy}/dB\right|_{B\sim 0\mathrm{T}}$, as this originates from a temperature independent carrier density.

Armed with the ordinary Hall effect we can readily extract the anomalous Hall effect as well as the magnetization (apart from the constant factor k):

$$R_{xy}^{AHE} = R_{xy} - R_{xy}^{OHE} \qquad \& \qquad kM_z = \frac{R_{xy} - R_{xy}^{OHE}}{R_s}$$

We plot both properties for four different samples in Figure S8. Most noticeable is that by combining the $R_{xy}(B)$ and $R_s(B)$ we obtain a plausible shape of the magnetization for all samples. This would by no means be obvious without applying the anomalous Hall effect theory, and it is, together with the correlation to the scanning SQUID images, a strong evidence that the anomalous Hall effect is the origin of the non-linear Hall effect. Further support is found when considering T = 2 K and B > 7 T where the magnetization is expected to be saturated. In this case, the anomalous Hall effect ($R_{xy}^{AHE} = R_s^{AHE}M_z$) scales linearly with the sheet resistance (R_s) as shown in Figure S9.

We note that the analysis render the low-field part of the magnetization particular prone to noise, and care should be taken when extracting information from this region.

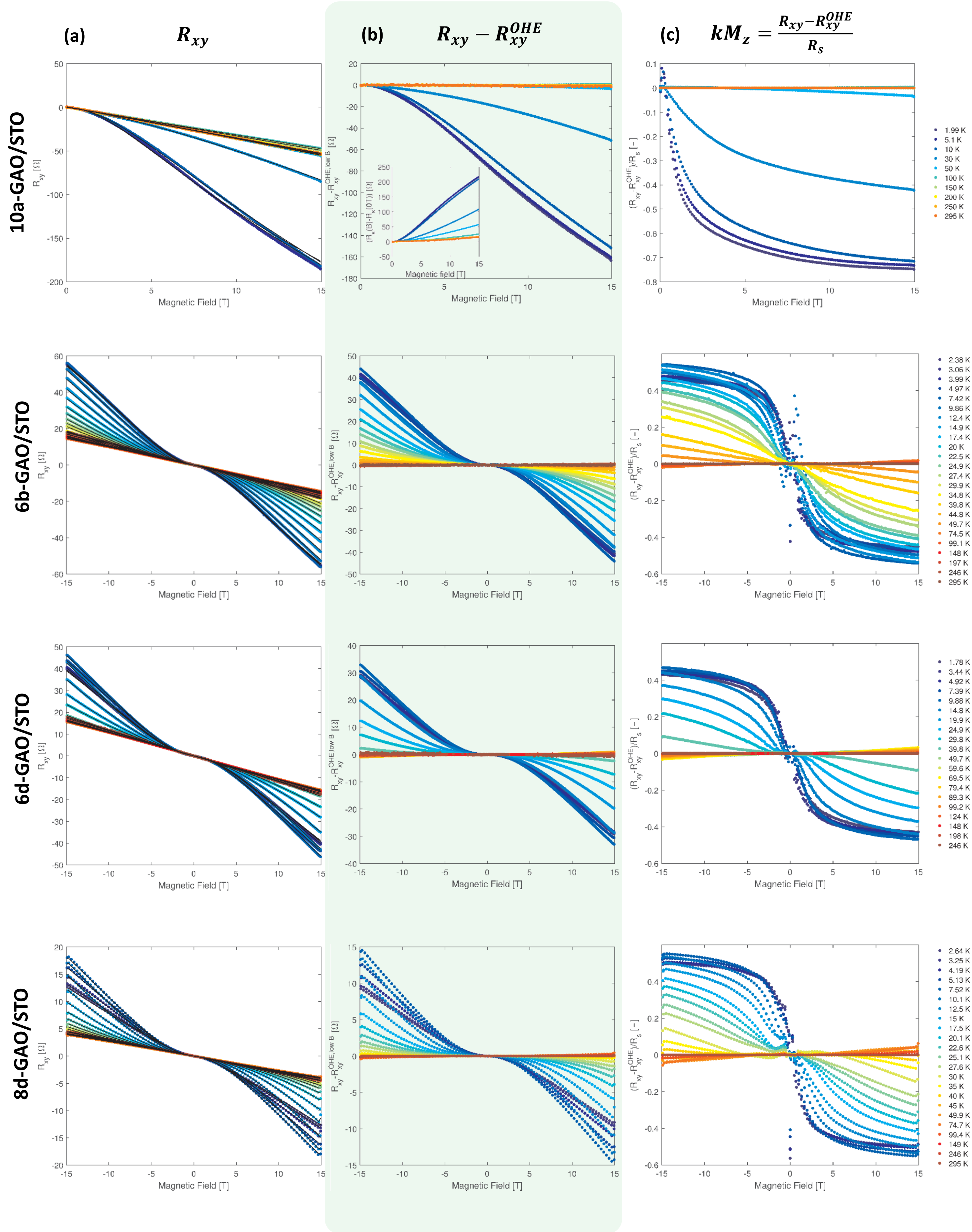

Figure S8: (a) Hall resistance (R_{xy}) as a function of magnetic field for four GAO/STO samples. (b) $R_{xy}^{AHE} = R_{xy} - R_{xy}^{OHE}$ where the ordinary Hall effect R_{xy}^{OHE} is defined as the low field slope of R_{xy}. For sample 10a, the sheet resistance (R_s) is shown for comparison. (c) By calculating $(R_{xy} - R_{xy}^{OHE})/R_s$ we obtain the component of the magnetization parallel to the magnetic field (M_z) multiplied by a constant factor k.

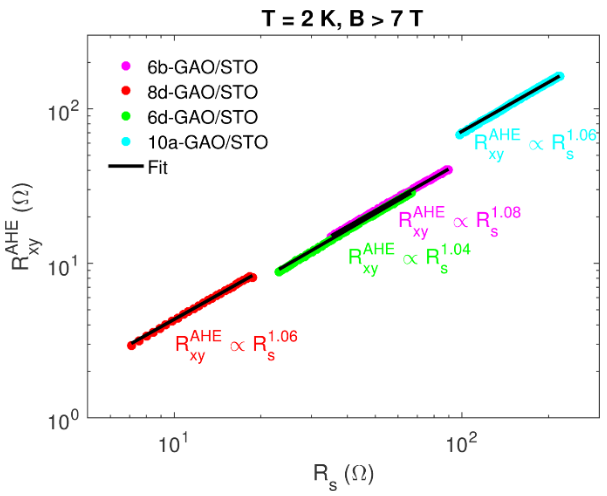

Figure S9: Anomalous Hall effect (R_{xy}^{AHE}) as a function of the sheet resistance (R_s) for four GAO/STO samples measured at low temperature and high magnetic field where the magnetization is expected to be saturated. Here, increasing the magnetic field results in a linear increase in both the magnetoresistance and the anomalous Hall effect.

Anomalous Hall effect with carrier transport in two n-type bands:

As outlined in Suppl. Section 5, we reject that the non-linear Hall effect results from simultaneous carrier transport in both an n-type and p-type band. In this section, we have instead concluded that the overall non-linearity in the Hall effect stems from the anomalous Hall effect. For simplicity, we described the ordinary Hall effect using a one band model. We here show that the conclusion remains unchanged if we consider carrier transport in two or more n-type bands. For the $SrTiO_3$-based heterostructures the two bands correspond to d_{xy} and d_{xz}/d_{yz} (*10, 19*).

1. Saturating R_S^{AHE}:

A two band conduction will contribute with an S-shaped Hall curve characterized by $\left|\lim_{B\to 0}\left(\frac{dR_{xy}}{dB}\right)\right| \geq \left|\lim_{B\to\infty}\left(\frac{dR_{xy}}{dB}\right)\right|$. The limit of $B \to \infty$ can be used to extract the total carrier density of the two bands using $\lim_{B\to\infty}(R_H) = -\frac{1}{e n_{s,\text{total}}}$ with $R_H = \frac{R_{xy}}{B}$. When discussing parameters derived from the high-field region, n_s can simply be replaced with $n_{s,\text{total}}$. Assuming a saturating R_S^{AHE} as above therefore implies the same predictions, namely a freeze-out in the total carrier density, a mobility increase as well as the same shape of $R_S^{AHE} M_S$.

2. Non-saturating R_S^{AHE}:

The anomalous Hall effect curve we derive is, to some extent, sensitive to whether we describe the ordinary Hall effect as an S-shaped curve (two band conduction) or a linear curve (single band conduction). However, since the S-shape has the opposite curvature with respect to the measured Hall data, the overall shape of the anomalous Hall curve will remain unchanged. Importantly, the conclusion that the overall non-linearity stems from the anomalous Hall effect with an onset temperature of 40 K remains also invariant to whether the ordinary Hall effect is described by transport in one or multiple n-type bands.

Section 7:
Kohler Plots

Signatures of magnetic ordering may be observed in the magnetoresistance. Many materials obey Kohler's rule (20), which predicts that the resistance ratio $R_s(B,T)/R_s(0,T)$ is some function f of $B/R_s(0,T)$.

$$\frac{R_s(B,T)}{R_s(B=0,T)} = F(\omega_c\tau) = f\left(\frac{B}{R_s\,(B=0,T)}\right)$$

Kohler's rule originates from the magnetic field entering the semi-classical Boltzmann equation as the product of the cyclotron frequency and scattering life time, $\omega_c\tau = eB\tau/m^*$ with m^* being the effective mass and τ generally being inversely proportional to R_s. As presented in Figure S10, Kohler's rule is obeyed in GAO/STO for $T > 40$ K, however, clear deviations are observed for $T < 40$ K, which coincides with the emergence of the non-linear Hall resistance. No hysteresis was detected in the magnetoresistance at any temperature. Deviations from Kohler's rule can have various origins (*21*). In the presence of magnetism, the electrons are scattered by spatially fluctuating magnetic moments leading to a negative magnetoresistance as increasing the magnetic field leads to alignment of the spins and lower degree of scattering. This scattering leads to a deviation of Kohler's rule as τ becomes dependent on B. In particular, we expect a lowering of the magnetoresistance at temperatures where spin scattering occurs compared to temperatures where the Kohler scaling is obeyed in the absence of high temperatures. This is also observed in Figure S10. Note that $\left(\frac{R_s(B)}{R_s(B=0)}\right)^{-1}$ is shown for convenience to put emphasis on the low-field part.

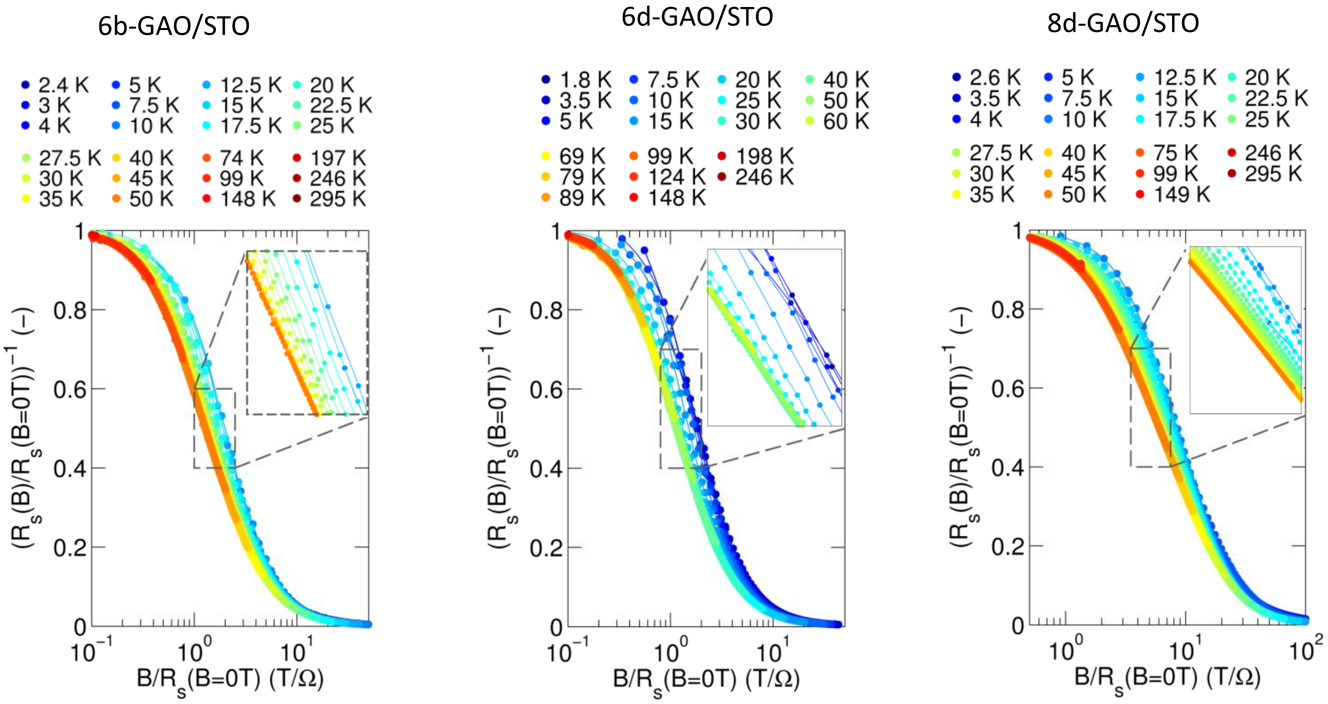

Figure S10: Kohler plots of three different samples showing deviations from the Kohler scaling below $T < 40$ K.

Section 8:
Mechanical tunability of the magnetic landscape of LAO/STO

Similar to the data presented in figure 3 in the main text, the magnetic stripes we observed in LAO/STO are also highly stress dependent (see Figure S11). At T = 15 K we observe no or weak modulations when we raster scan the SQUID across the sample in non-contact mode. After contacting the sample with the tip of the scanning probe, we observe stronger stripy modulations of the magnetic signal. These modulations grow stronger as we increase the applied force.

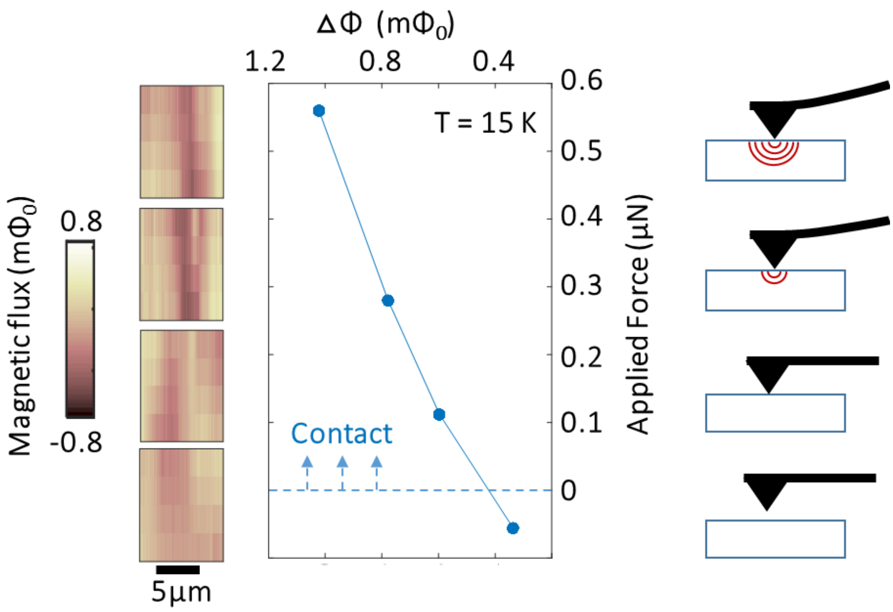

Figure S11: Magnetic modulation vs. force applied with the scanning SQUID tip at T = 15 K. No or weak modulations are observed before contacting the sample. As we increase the force applied to the sample by the tip, the magnetic modulations become stronger. The left column shows 2D maps of the measured magnetic flux where the probe applies different forces to the sample surface. For convenience, the peak-to-peak modulation amplitude (ΔΦ) is also shown in the middle panel. The magnetic flux is offset by the average value of the scan for all figures.

Section 9:
Local susceptibility measurements vs. temperature and pressure

We apply magnetic fields locally using the scanning SQUID field coil and measure how it modulates the magnetic signal from the sample, as in Figure 3 of the main text. The magnetic susceptibility shows similar behavior with stress and temperature as the magnetometry data. Below ~8 K only minor modulations are observed, whereas above 8 K the susceptibility signal increases rapidly. We observe that there are small areas where the susceptibility signal grows slower as the temperature and stress are increased. We suggest that the magnetic moments in most areas gradually convert into paramagnetic moment and therefore show an increase in the susceptibility. At the domain walls (the small areas), the magnetic moments remain largely ordered and therefore show a reduced growth in the magnetic susceptibility as well as a large D.C. magnetic signal in absence of an external magnetic field.

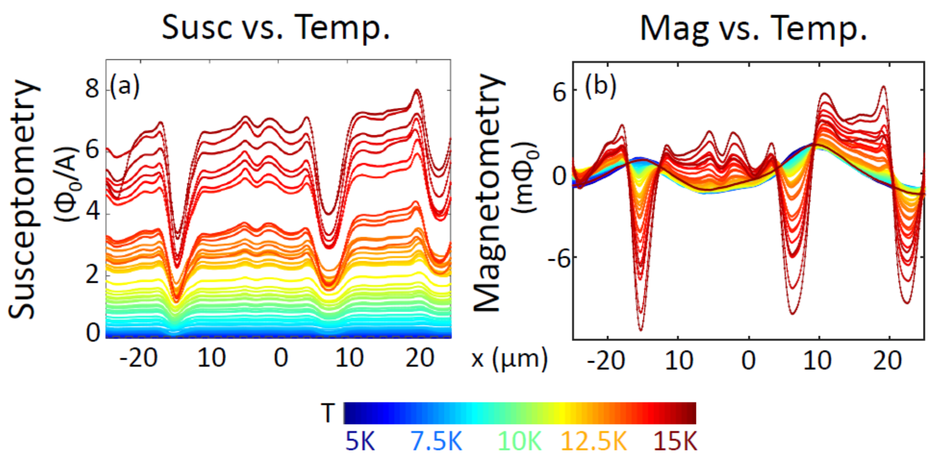

Figure S12: Magnetic and susceptibility measurements as a function of temperature. The measurements were performed on GAO/STO with an applied force of 56nN in the same locations as in Figure 3 in the main text. (a) Susceptibility measurements primarily showing an increasing paramagnetic signal as the temperature is increased. Smaller segments that we attribute to the domain walls show a slower increase of the paramagnetic signal with temperature. (b) Magnetometry measurements showing an increase in the modulation magnitude with temperature in absence of an applied magnetic field. We detect stronger magnetic signal on the small segments attributed to domain walls. (a) and (b) were measured simultaneously.

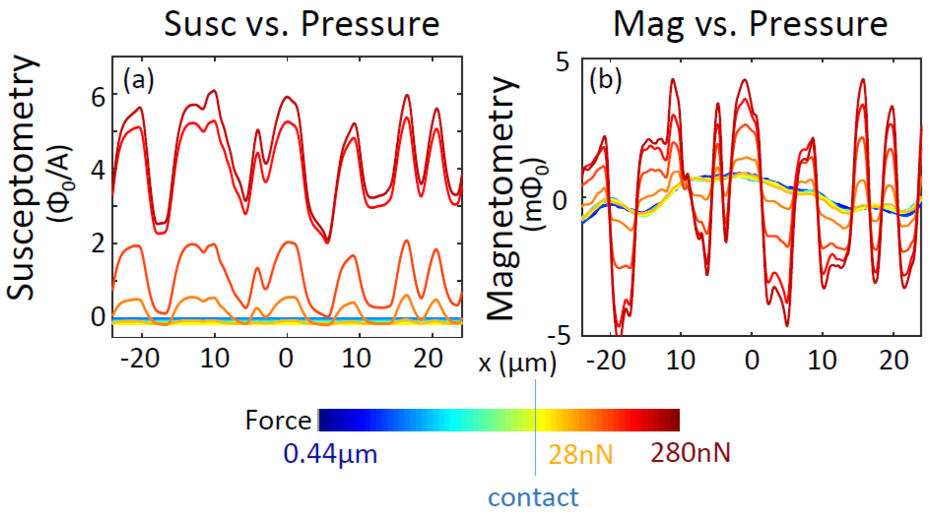

Figure S13: Magnetic and susceptibility measurements as a function of applied pressure. The measurements were performed at 17 K on GAO/STO at a different location compared to Figure S12. (a) Susceptibility measurements showing small segments attributed to the domain walls showing a slower increase of the paramagnetic signal as the applied pressure is increased. (b) Magnetometry measurements showing that the magnetic modulations become stronger as the pressure is increased. We detect stronger magnetic signal on the small segments attributed to domain walls. (a) and (b) were measured simultaneously.

Section 10:
References

1. J. A. Bert *et al.*, Direct imaging of the coexistence of ferromagnetism and superconductivity at the $LaAlO_3/SrTiO_3$ interface. *Nat. Phys.* **7**, 767–771 (2011).

2. D. V. Christensen *et al.*, Electric field control of the γ-$Al_2O_3/SrTiO_3$ interface conductivity at room temperature. *Appl. Phys. Lett.* **109**, 021602 (2016).

3. M. E. Huber *et al.*, Gradiometric micro-SQUID susceptometer for scanning measurements of mesoscopic samples. *Rev. Sci. Instrum.* **79**, 053704 (2008).

4. J. R. Kirtley *et al.*, Scanning SQUID susceptometry of a paramagnetic superconductor. *Phys. Rev. B.* **85**, 224518 (2012).

5. Y. Frenkel *et al.*, Imaging and tuning polarity at $SrTiO_3$ domain walls. *Nat. Mater.* **16**, 1203–1208 (2017).

6. J. M. D. Coey, M. Venkatesan, P. Stamenov, Surface magnetism of strontium titanate. *J. Phys. Condens. Matter.* **28**, 485001 (2016).

7. B. Kalisky *et al.*, Locally enhanced conductivity due to the tetragonal domain structure in $LaAlO_3/SrTiO_3$ heterointerfaces. *Nat. Mater.*, 1091–1095 (2013).

8. D. V. Christensen *et al.*, Electron Mobility in γ-$Al_2O_3/SrTiO_3$. *Phys. Rev. Appl.* **9**, 054004 (2018).

9. M. Ben Shalom, A. Ron, A. Palevski, Y. Dagan, Shubnikov–De Haas Oscillations in $SrTiO_3/LaAlO_3$ Interface. *Phys. Rev. Lett.* **105**, 206401 (2010).

10. A. Joshua, S. Pecker, J. Ruhman, E. Altman, S. Ilani, A universal critical density underlying the physics of electrons at the $LaAlO_3/SrTiO_3$ interface. *Nat. Commun.* **3**, 1129 (2012).

11. F. Gunkel *et al.*, Defect Control of Conventional and Anomalous Electron Transport at Complex Oxide Interfaces. *Phys. Rev. X.* **6**, 031035 (2016).

12. A. Joshua, J. Ruhman, S. Pecker, E. Altman, S. Ilani, Gate-tunable polarized phase of two-dimensional electrons at the $LaAlO_3/SrTiO_3$ interface. *Proc. Natl. Acad. Sci.* **110**, 9633–9638 (2013).

13. D. V. Christensen *et al.*, Controlling the carrier density of $SrTiO_3$-based heterostructures with annealing. *Adv. Electron. Mater.*, 1700026 (2017).

14. N. Nagaosa, J. Sinova, S. Onoda, A. H. MacDonald, N. P. Ong, Anomalous Hall effect. *Rev. Mod. Phys.* **82**, 1539–1592 (2010).

15. M. Yazdi-Rizi *et al.*, Infrared ellipsometry study of the confined electrons in a high-mobility γ-$Al_2O_3/SrTiO_3$ heterostructure. *EPL Europhys. Lett.* **113**, 47005 (2016).

16. E. Mikheev *et al.*, Limitations to the room temperature mobility of two- and three-dimensional electron liquids in $SrTiO_3$. *Appl. Phys. Lett.* **106**, 062102 (2015).

17. P. Irvin *et al.*, Anomalous High Mobility in $LaAlO_3/SrTiO_3$ Nanowires. *Nano Lett.* **13**, 364–368 (2013).

18. A. Ohtomo, H. Y. Hwang, A high-mobility electron gas at the $LaAlO_3/SrTiO_3$ heterointerface. *Nature*. **427**, 423–426 (2004).

19. Y. Cao *et al.*, Anomalous orbital structure in a spinel–perovskite interface. *Npj Quantum Mater.* **1**, 16009 (2016).

20. A. B. Pippard, *Magnetoresistance in metals* (Cambridge University Press, ed. 1st, 1989).

21. R. H. McKenzie, J. S. Qualls, S. Y. Han, J. S. Brooks, Violation of Kohler's rule by the magnetoresistance of a quasi-two-dimensional organic metal. *Phys. Rev. B*. **57**, 11854 (1998).